

Klein tunneling in deformed $\alpha - T_3$ lattice

L. Mandhour* and F. Bouhadida

*Laboratoire de Physique de la Matière Condensée,
Faculté des Sciences de Tunis, Université de Tunis el Manar,
Campus Universitaire Tunis, El Manar, 2092 Tunis, Tunisie.*

(Dated: June 3, 2020)

By applying a compressive uniaxial deformation on the $\alpha - T_3$ lattice, which interpolates between honeycomb lattice ($\alpha = 0$) and dice lattice ($\alpha = 1$), the Dirac cones move toward each other along a given direction, merge and a gap opens while the flat band remains unchanged. Therefore, the low-energy spectrum, along this merging direction, exhibits a transition from a linear dispersion in the Dirac phase to a quadratic dispersion in the gapped phase. However, along the perpendicular direction the spectrum remains linear. Here we theoretically study the tunneling properties of particles through a np junction in deformed $\alpha - T_3$ lattice. In the Dirac phase, we find that the tunneling properties are similar to those of undeformed $\alpha - T_3$ lattice such as the perfect Klein tunneling at normal incidence for all values of α and the total transparency of the junction, i.e. the super-Klein tunneling, for $\alpha = 1$ when the energy is equal to half of the junction height. In the gapped phase, we obtain an opposite behavior when the junction is oriented perpendicular to the deformation direction where the perfect Klein tunneling turns into the anti-Klein tunneling effect for all parameters α and the super-Klein tunneling effect transits to the anti-super Klein tunneling effect, i.e. the junction is totally opaque.

I. INTRODUCTION

The Klein tunneling (KT) manifests as the perfect transmission of relativistic particles perpendicular to a potential barrier of height greater than twice the rest energy mc^2 of the particle (where m is the mass and c is the speed of light) [1–3]. Therefore, the experimental realization of the KT in physics particles is unreachable due to the requirement of an enormous electric field. The discovery of graphene [4], a single sheet of carbon atoms arranged in a honeycomb lattice (HCL), has allowed the experimental realization of the KT in condensed matter systems [5–7]. This is due to the fact that particles in graphene behave as chiral massless Dirac fermions with pseudospin-1/2 which is conserved across the interface of the barrier [8, 9].

The KT occurs in relativistic materials satisfying the Dirac-Weyl equation with enlarged pseudospin $S > 1/2$ [10, 11]. Particularly, a striking transport property observed in pseudospin-1 systems is the omnidirectional perfect transmission, called super-Klein tunneling (SKT), for an energy equal to half of the junction height [12–16]. It has been reported that SKT is also possible in pseudospin-1/2 Dirac materials [17]. The dice lattice or T_3 [18–20], an example of pseudospin-1 systems, presents the same structure as HCL with an additional site at the center of each hexagon. The low-energy behavior of the dice lattice is governed by the same Dirac-Weyl Hamiltonian as graphene, but with pseudospin $S = 1$. The corresponding low energy band structure is similar to that of HCL with an additional flat band at the Dirac points. The $\alpha - T_3$ model was introduced by A. Raoux *et al.* [21] to interpolate between the HCL ($\alpha = 0$) and the dice lattice ($\alpha = 1$). In this lattice, the low-energy behavior is governed by the Dirac-Weyl Hamiltonian with an hybrid pseudospin $S = 1/2 - 1$ [22]. E. Illes *et al.* [10]

have studied the Klein tunneling in the $\alpha - T_3$ model and have found a perfect transmission at normal incidence for all the values of α and showed that the transmission is enhanced with increasing α for other angles of incidence. A paper by Malcolm and Nicol [23] showed that $Hg_{1-x}Cd_xTe$, for a critical value $x \approx 0.17$, maps onto the $\alpha - T_3$ structure for a parameter $\alpha = \frac{1}{\sqrt{3}}$.

In contrast to monolayer graphene, particles in bilayer graphene behave as chiral massive Dirac fermions and exhibit total reflection when normally incident on a potential barrier. This effect, known as anti-Klein tunneling (AKT) [8, 24–26], is a consequence of the pseudospin conservation between incident and reflected particles. The AKT is also possible in other relativistic materials such as deformed honeycomb lattice [27], graphene in the presence of strong Rashba spin-orbit coupling [28] and semi-Dirac materials [29]. Omni-directional perfect reflection, the counterpart of the SKT found in pseudospin-1 systems, has been observed in phosphorene [30]. This effect, called anti-super-Klein tunneling (ASKT), is related to the fact that the pseudospins of the incident and transmitted electrons are antiparallel.

Under the effect of a uniaxial deformation on the HCL the Dirac points are shifted away from the K and K' valleys. For a sufficiently strong deformation, the two Dirac points merge into a single one and a gap opens [31–37]. This merging of Dirac points signals a topological transition from a semi-metallic to an insulating phase. Therefore, the low-energy spectrum, along this merging direction, exhibits a transition from linear to quadratic dispersion while the dispersion remains linear along the perpendicular direction. Particularly, at the merging point, known as semi-Dirac point [38], the dispersion is linear in one direction and quadratic in the other. In a tight-binding picture, the moving and the merging of Dirac points can be made by tuning one of the

three nearest-neighbor hopping parameters in a HCL[32] which is not possible in graphene due to its high stiffness [33]. However the merging of the Dirac points may be observed in other graphene-like systems, known as artificial graphenes [39], such as ultracold atoms trapped in a honeycomb optical lattice [36], microwave photonic crystals[40] and for a review see [41].

The effect of the deformation of HCL on the electronic transport has been investigated [27, 29, 42–45]. A transition from KT to AKT has been reported in such deformed HCL by controlling the strength[27] or the direction[29, 43] of the deformation. This is related to the effective mass of the Dirac fermions who undergoes a transition from massless to massive Dirac fermions. This transition has been studied in other materials such as double-Weyl semimetals [47] and bilayer graphene [26, 46, 48]. To the best of our knowledge, the transition from SKT to ASKT has not been studied.

In this paper, we theoretically study the Klein tunneling in a deformed $\alpha - T_3$ lattice. We focus on the effects of the deformation and the parameter α on the transmission across a np junction. When the junction is oriented perpendicular to the deformation direction, we distinguish three phases when a continuous compressive uniaxial deformation is applied on the $\alpha - T_3$ lattice. The first, namely the Dirac phase, where we show that tunneling properties across the np junction such as KT, SKT and the α -dependent transparency of the junction are similar to those reported in the undeformed $\alpha - T_3$ model[10]. In the second phase, called the semi-Dirac phase, we notice that the intervalley scattering destroys the KT and the SKT found in the Dirac phase. When the Dirac cones merge, the regime of AKT is observed when the junction is perpendicular to the deformation direction for all the values of α . Interestingly, a transition from the SKT to the ASKT in the dice lattice ($\alpha = 1$) can be realized by the rotation of the junction at the merging point or by a continuous uniaxial deformation perpendicular to the junction.

The paper is organized as follows. In section II, we introduce the deformed $\alpha - T_3$ model and discuss the influence of the uniaxial deformation on the energy spectrum and the wave functions. In section III, we present the transmission probability and the conductance calculations in the three phases and for the two orientations of the np junction with respect to the deformation direction. In section IV, we show and discuss our results. Conclusions are given in Section V.

II. LOW-ENERGY BAND DISPERSION OF THE DEFORMED $\alpha - T_3$ MODEL

Graphene is characterized by a honeycomb lattice (HCL) formed by a regular arrangement of two sites, labeled A and B , connected with a hopping amplitude t . Starting from HCL lattice, the dice lattice (T_3) is obtained by adding a site C , in the center of each hexagon,

connected to one of the two inequivalent sites (for example B) with a hopping amplitude $t_{BC} = t_{AB} = \frac{t}{\sqrt{2}}$.

In the $\alpha - T_3$ lattice, the site B is coupled to the three A sites via the hopping amplitude $t_{AB}^{\vec{\delta}_i} = t \cos \varphi$ and to the three C sites via the hopping amplitude $t_{BC}^{-\vec{\delta}_i} = t \sin \varphi$, where $\vec{\delta}_i (i = 1, 2, 3)$ are the vectors connecting the nearest-neighbors sites. By applying a compressive uniaxial deformation on the $\alpha - T_3$ lattice along the $\vec{\delta}_1$ direction (y direction), the corresponding hopping amplitudes are modified and they are, respectively, given by: $t_{AB}^{\vec{\delta}_1} = \lambda t_{AB}^{\vec{\delta}_1}$ and $t_{BC}^{-\vec{\delta}_1} = \lambda t_{BC}^{-\vec{\delta}_1}$ (see Fig.1). The parameter $\lambda \geq 1$ measures the strength of the lattice deformation.

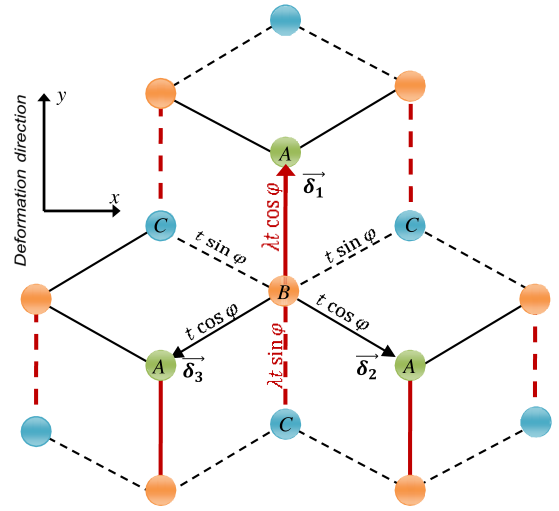


FIG. 1. (Color online) Schematic representation of the deformed $\alpha - T_3$ lattice. There are three sites A , B and C in each unit cell. The hopping amplitudes between A and B sites are $\lambda t \cos \varphi$ ($\lambda > 1$) along the deformation direction (red thick lines) and $t \cos \varphi$ in the other directions (black thin lines). The hopping amplitude connecting B to C is $\lambda t \sin \varphi$ along the deformation direction (red dashed thick lines) and $t \sin \varphi$ (black dashed thin lines) in the other directions.

Following the nearest-neighbor tight-binding model, the Hamiltonian describing the electronic properties of this system reads as follows [21, 50]:

$$H_o = \begin{pmatrix} 0 & \cos \varphi f_\lambda(\vec{k}) & 0 \\ \cos \varphi f_\lambda^*(\vec{k}) & 0 & \sin \varphi f_\lambda(\vec{k}) \\ 0 & \sin \varphi f_\lambda^*(\vec{k}) & 0 \end{pmatrix} \quad (1)$$

where $f_\lambda(\vec{k}) = t(\lambda e^{-i\vec{k}\vec{\delta}_1} + e^{-i\vec{k}\vec{\delta}_2} + e^{-i\vec{k}\vec{\delta}_3})$ [50]. $\vec{\delta}_1 = a\vec{e}_y$, $\vec{\delta}_2 = \frac{a}{2}(\sqrt{3}\vec{e}_x - \vec{e}_y)$ and $\vec{\delta}_3 = \frac{a}{2}(-\sqrt{3}\vec{e}_x - \vec{e}_y)$ are the vectors connecting the nearest-neighbors sites with a is the intersite distance.

The energy spectrum consists of a flat band $E = 0$ and two dispersive bands $E = s |f_\lambda(\vec{k})|$, where $s = \pm$ is the

band index. The corresponding eigenfunctions read:

$$\Psi_\lambda^0(\vec{r}) = \begin{pmatrix} \sin\varphi e^{i\theta_\lambda} \\ 0 \\ -\cos\varphi e^{-i\theta_\lambda} \end{pmatrix} e^{i\vec{k}\vec{r}} \quad (2a)$$

$$\Psi_\lambda^s(\vec{r}) = \frac{1}{\sqrt{2}} \begin{pmatrix} \cos\varphi e^{i\theta_\lambda} \\ s \\ \sin\varphi e^{-i\theta_\lambda} \end{pmatrix} e^{i\vec{k}\vec{r}} \quad (2b)$$

where the phase $\theta_\lambda = \arg(f_\lambda(\vec{k}))$.

The particularity of this model, for a given λ , is that the energy spectrum is independent of the parameter α which is not the case for the eigenfunctions.

Let us now discuss the effect of the strength of deformation λ on the band structure of the deformed $\alpha - T_3$ lattice. For $\lambda = 1$, we are in the case of the undeformed $\alpha - T_3$ lattice. The energy band spectrum, at low energy, is described by linear bands touching at the K and K' valleys of the Brillouin zone. This situation is similar to that encountered in graphene but with an additional flat band at $E = 0$ [21]. In the case of $1 < \lambda < 2$, the Dirac cones are no longer at the K and K' points but approach each other along the k_x direction as λ increases. The new positions of Dirac points D_\pm are determined from the condition $f_\lambda(\vec{k}_{D_\pm}) = 0$. When $\lambda = 2$, the Dirac points D_\pm merge into the $M\left(\frac{2\pi}{a\sqrt{3}}, 0\right)$ point and a gap opens for $\lambda > 2$.

Here, we are interested on the low energy hamiltonian. At the vicinity of the Dirac points D_ξ ($\xi = \pm$) with $1 \leq \lambda \leq 2$, the function $f_\lambda(\vec{k})$ is given by:

$$f_\lambda(\vec{k} + \vec{D}_\xi) = \frac{\hbar^2 \delta k_x^2}{2m} + \xi \hbar v_x \delta k_x - i \hbar v_y \delta k_y \quad (3)$$

where $m = \frac{4\hbar^2}{3\lambda a^2 t}$ and the velocities along the x and y directions read:

$$v_x = \sqrt{\frac{4 - \lambda^2}{3}} v_F, \quad v_y = \lambda v_F \quad (4)$$

with $v_F = \frac{3at}{2\hbar}$ is the Fermi velocity in the undeformed lattice [31]. We have included the quadratic term in δk_x because the linear term vanishes when λ approaches 2 [27]. For $\lambda > 2$ the term v_x becomes imaginary and the corresponding Hamiltonian cannot describe the system. Thereafter, we write the function $f_\lambda(\vec{k})$ around the M point by making the change $k_x = \delta k_x - k_M$, $k_y = \delta k_y$:

$$f_\lambda(\vec{k}) = \Delta + \frac{\hbar^2 k_x^2}{2m} - i \hbar v_y k_y \quad (5)$$

where $k_M = \frac{\xi m v_x}{\hbar}$ is the position of the D_ξ point relatively to the M point and $\Delta = \frac{\lambda^2 - 4}{2\lambda} t$ is the gap parameter. The Hamiltonian (1) with $f_\lambda(\vec{k})$ given by Eq. (5)

describes the physics of the system for all the values of $\lambda \geq 1$ and can be written as:

$$H_o = \left(\Delta + \frac{\hbar^2 k_x^2}{2m} \right) S_x^\varphi + \hbar v_y k_y S_y^\varphi \quad (6)$$

where the pseudospin matrices read:

$$S_x^\varphi = \begin{pmatrix} 0 & \cos\varphi & 0 \\ \cos\varphi & 0 & \sin\varphi \\ 0 & \sin\varphi & 0 \end{pmatrix} \quad (7)$$

$$S_y^\varphi = i \begin{pmatrix} 0 & -\cos\varphi & 0 \\ \cos\varphi & 0 & -\sin\varphi \\ 0 & \sin\varphi & 0 \end{pmatrix}$$

Note that this Hamiltonian reproduces the universal Hamiltonian obtained by G. Montambaux *et al.* [32] in the case of graphene ($\alpha = 0$).

The variation of Δ (or λ) gives rise to three distinct phases as shown in Fig. 2. For $\Delta < \Delta_o < 0$ and an energy $E \ll |\Delta|$, we can neglect the quadratic term in δk_x from Eq. (3) and the low energy spectrum is formed by two separate Dirac cones located at D_\pm with a flat band (Fig.2) which is called the Dirac phase [44]. In this case, the Dirac cones are anisotropic with different velocities in the x and y directions (Eq. (4)) where the particles behave as massless Dirac fermions. For $\Delta_o < \Delta \leq 0$ and an energy $E \sim |\Delta|$, we are in the semi-Dirac phase, the linear and quadratic terms in Eq. (3) indicate the coexistence of massless and massive particles in the x direction. The gapped phase appears for $\Delta > 0$ where the particles are massive along the x direction. Particularly, at $\Delta = 0$, the band structure is linear in the k_y direction and parabolic in the k_x direction with a flat band $E = 0$ (Fig.2) which is called the $\alpha - T_3$ semi-Dirac model [50]. Note that the dispersion relation is linear along the y direction in all phases as depicted in Fig. 2 and the particles behave as massless Dirac fermions. Finally, the flat band is robust to the deformation.

III. TRANSMISSION PROBABILITY

We study the particle transmission through a potential step (*np* junction) of a height V_0 with two orientations: parallel (y axis) and perpendicular (x axis) to the deformation direction.

A. Tunneling along the x direction:

Here, we calculate the transmission probability across the *np* junction perpendicular to the deformation direction (along the x direction) in the three phases shown in Fig. 2. The potential is modeled by:

$$V(x) = V_o \Theta(x) \quad (8)$$

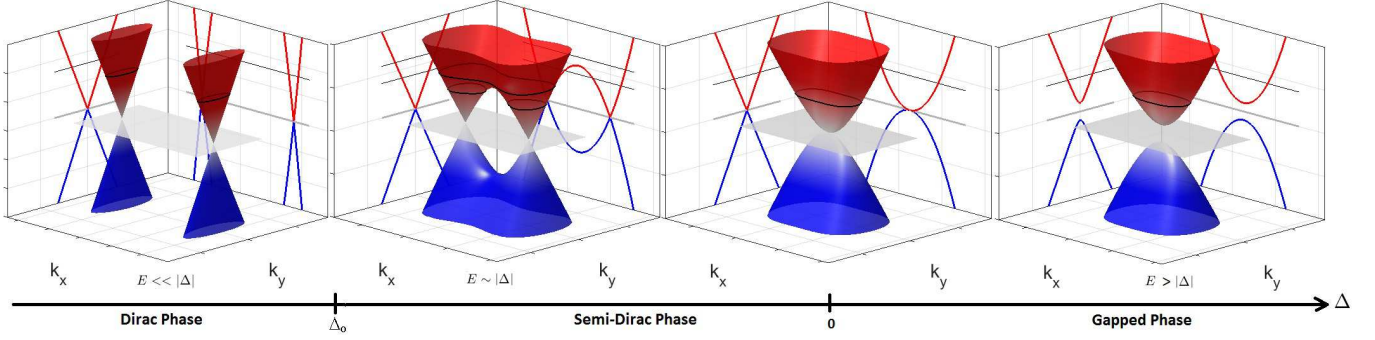


FIG. 2. (Color online) The energy spectrum of the deformed $\alpha - T_3$ model for various Δ (or λ). The black lines indicate the energy E of the particles. The Dirac phase: $\Delta < \Delta_o < 0$ and $E \ll |\Delta|$. The semi-Dirac phase: $\Delta_o < \Delta \leq 0$ and $E \sim |\Delta|$. The gapped phase: $E > \Delta > 0$.

where $\Theta(x)$ is the Heaviside step function.

The potential step is sharp but is assumed to vary over a length scale larger than the in-plane interatomic distance and smaller than the electron wavelength so that it does not induce the intervalley scattering. The potential step is uniform along the y direction so that the y component of the wave vector is conserved. The wave function can thus be written as $\Psi(x, y) = \psi(x) e^{ik_y y}$. Solving the Schrödinger equation $[H_o + V(x)] \psi(x) = E \psi(x)$ with the Hamiltonian (6) for a given energy $0 < E < V_o$, the transverse momentum k_y and the gap parameter Δ , there are four possible longitudinal momenta $k_x^{\xi\eta} = \xi k_{x\eta}$ ($q_x^{\xi\eta} = \xi q_{x\eta}$) in region n (p) which are written as:

$$k_{x\eta} = \sqrt{\frac{2m}{\hbar^2}} \sqrt{-\Delta + \eta \sqrt{E^2 - \hbar^2 v_y^2 k_y^2}} \quad (9)$$

$$q_{x\eta} = \sqrt{\frac{2m}{\hbar^2}} \sqrt{-\Delta + \eta \sqrt{(E - V_o)^2 - \hbar^2 v_y^2 k_y^2}}$$

where $\xi = \pm$ denotes the two Dirac points and $\eta = \pm$ indicates the two longitudinal momenta $k_{x\pm}$ (or $q_{x\pm}$) on both sides of a Dirac point. This wave vector can be real or imaginary representing respectively a traveling or an evanescent wave. The corresponding normalized eigenstates in the n and p regions are of the form:

$$\psi_n^{(\xi\eta)}(x) = \frac{1}{\sqrt{2}} \begin{pmatrix} \cos \varphi e^{i\theta\eta} \\ 1 \\ \sin \varphi e^{-i\theta\eta} \end{pmatrix} e^{ik_x^{\xi\eta} x} \quad (10a)$$

$$\psi_p^{(\xi\eta)}(x) = \frac{1}{\sqrt{2}} \begin{pmatrix} \cos \varphi e^{i\phi\eta} \\ -1 \\ \sin \varphi e^{-i\phi\eta} \end{pmatrix} e^{iq_x^{\xi\eta} x} \quad (10b)$$

where $\cos \theta\eta = \eta \cos \theta$, $\sin \theta\eta = -\sin \theta$, $\cos \phi\eta = \eta \cos \phi$ and $\sin \phi\eta = -\sin \phi$ with:

$$\theta = \arg \left[\sqrt{E^2 - \hbar^2 v_y^2 k_y^2} + i\hbar v_y k_y \right] \quad (11)$$

$$\phi = \arg \left[\sqrt{(E - V_o)^2 - \hbar^2 v_y^2 k_y^2} + i\hbar v_y k_y \right]$$

These phases indicate the directions of the pseudospins in the n and p regions (see Fig. 3) which are given by:

$$\begin{aligned} \langle S_x \rangle_n^\eta &= \langle \psi_n^{\xi\eta} | S_x^\varphi | \psi_n^{\xi\eta} \rangle = \eta \cos \theta \\ \langle S_x \rangle_p^\eta &= \langle \psi_p^{\xi\eta} | S_x^\varphi | \psi_p^{\xi\eta} \rangle = -\eta \cos \phi \\ \langle S_y \rangle_n^\eta &= \langle \psi_n^{\xi\eta} | S_y^\varphi | \psi_n^{\xi\eta} \rangle = \sin \theta \\ \langle S_y \rangle_p^\eta &= \langle \psi_p^{\xi\eta} | S_y^\varphi | \psi_p^{\xi\eta} \rangle = -\sin \phi \end{aligned} \quad (12)$$

When $k_x^{\xi\eta}$ and $q_x^{\xi\eta}$ are real, the corresponding group velocities along the x direction in regions n and p are given by:

$$v_{xn}^{\xi\eta} = \frac{1}{\hbar} \frac{\partial E}{\partial k_x^{\xi\eta}} = \frac{\hbar}{m} \frac{\xi\eta}{E} k_{x\eta} \sqrt{E^2 - \hbar^2 v_y^2 k_y^2}$$

$$v_{xp}^{\xi\eta} = \frac{1}{\hbar} \frac{\partial (E - V_o)}{\partial q_x^{\xi\eta}} = \frac{\hbar}{m} \frac{\xi\eta q_{x\eta}}{(E - V_o)} \sqrt{(E - V_o)^2 - \hbar^2 v_y^2 k_y^2} \quad (13)$$

which take respectively the signs of $\frac{\xi\eta}{E}$ and $\frac{\xi\eta}{(E - V_o)}$. These group velocities are related to the pseudospins as:

$$v_{xn}^{\xi\eta} = \frac{\hbar}{m} \xi k_{x\eta} \langle S_x \rangle_n^\eta \quad (14)$$

$$v_{xp}^{\xi\eta} = \frac{\hbar}{m} \xi q_{x\eta} \langle S_x \rangle_p^\eta$$

There are three situations of the topology of the Fermi surfaces in each region as depicted in Fig. 3:

(i) When $0 < E < -\Delta$ ($0 < |E - V_o| < -\Delta$) the two Fermi surfaces are disconnected (Fig. 3 (a)) in region n (p). In this case the two longitudinal momenta $k_{x\pm}$ ($q_{x\pm}$) are real when $|k_y| < k_{max} = \frac{E}{\hbar v_y}$ ($|k_y| < q_{max} = \frac{|E - V_o|}{\hbar v_y}$).

(ii) When $E > -\Delta > 0$ ($|E - V_o| > -\Delta > 0$) the Fermi surfaces are partially connected in region n (p) (Fig. 3 (b)). For the case where $|k_y| < k_{in} = \frac{\sqrt{E^2 - \Delta^2}}{\hbar v_y}$ ($|k_y| < q_{in} = \frac{\sqrt{(E - V_o)^2 - \Delta^2}}{\hbar v_y}$) the Fermi surfaces are connected in region n (p) and the longitudinal momentum k_{x-} (q_{x-}) becomes imaginary while k_{x+} (q_{x+}) remains real. In the other case when $k_{in} < |k_y| < k_{max}$

the Fermi surfaces are partially connected in region n (p) and the longitudinal momentum k_{x-} (q_{x-}) becomes imaginary while k_{x+} (q_{x+}) remains real. In the other case when $k_{in} < |k_y| < k_{max}$

($q_{in} < |k_y| < q_{max}$) the Fermi surfaces are disconnected as in (i).

(iii) In the gapped phase ($E > \Delta \geq 0$ and $|E - V_o| > \Delta \geq 0$) the Fermi surfaces are disconnected in the two regions (Fig. 3 (c)). In this case the longitudinal momentum k_{x+} (q_{x+}) is real when $|k_y| < k_{in}$ ($|k_y| < q_{in}$) while k_{x-} (q_{x-}) becomes imaginary.

We also represent in Fig. 3 the group velocities and the pseudospin texture along the Fermi surfaces in the two regions n and p .

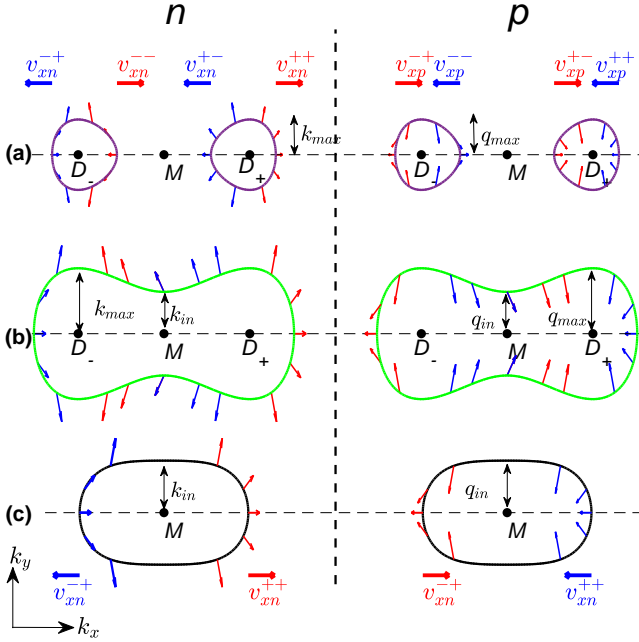


FIG. 3. (Color online) Fermi surfaces topology and pseudospin texture in the two regions n and p . Red and blue denote respectively the forward and backward propagation given from the group velocities $v_{xn}^{\xi\eta}$ and $v_{xp}^{\xi\eta}$ along the x direction (Eq. (13)). (a) The Fermi surfaces are disconnected. (b) The Fermi surfaces are partially connected. (c) The Fermi surfaces are disconnected.

The tunneling across the np junction depends on the topology of the Fermi surfaces in the two regions as illustrated in Fig. 4. In the case where the Fermi surfaces are disconnected in the two regions ($k_{x\pm}$ and $q_{x\pm}$ are real) there are four transmission channels (Fig. 4 (a)). In the gapped phase the two Fermi surfaces are connected in the two regions n and p leading to one transmission channel because the momentum k_{x-} and q_{x-} become imaginary (Fig. 4 (e)). In the semi-Dirac phase (Fig. 4(b-d)) the Fermi surfaces can be connected or disconnected in the two regions or connected in one region and disconnected in the other for a given incident angle (as controlled by transverse momentum k_y). For example in Fig. 4 (b) there are two transmission channels T^\pm when the Fermi surfaces are connected in region p ($|k_y| < q_{in}$) and four transmission channels (as in (a)) when the Fermi surfaces are disconnected ($q_{in} < |k_y| < q_{max}$).

The different transmission probabilities can be deduced from the case where the Fermi surfaces are disconnected in the two regions. In this case the total wave function is given by:

$$\begin{aligned}\psi(x < 0) &= \psi_n^{(\xi\xi)}(x) + r_\xi^\xi \psi_n^{(\xi-\xi)}(x) + r_{-\xi}^\xi \psi_n^{(-\xi\xi)}(x) \\ \psi(x > 0) &= t_\xi^\xi \psi_p^{(\xi-\xi)}(x) + t_{-\xi}^\xi \psi_p^{(-\xi\xi)}(x)\end{aligned}\quad (15)$$

where t_ξ^ξ ($t_{-\xi}^\xi$) is the intravalley (intervalley) transmission amplitude (see Fig. 4 (a)) and the same for the reflection amplitudes r_ξ^ξ and $r_{-\xi}^\xi$. The wave functions $\psi_{n,p}^{(\xi\xi')}(x)$ are given from Eq. (10a) and Eq. (10b). a step function In order to obtain the transmission and reflection ampli-

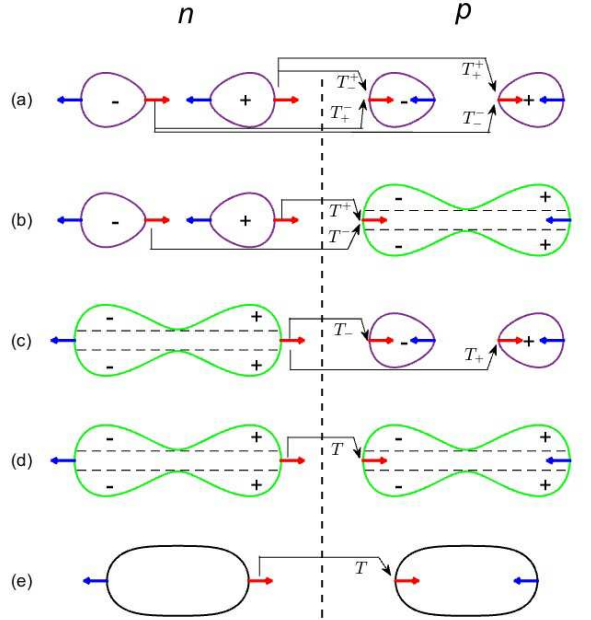


FIG. 4. (Color online) Schematic representation of the transmission probabilities for different topologies of the Fermi surfaces. The arrows represent the group velocities $v_{xn}^{\xi\eta}$ and $v_{xp}^{\xi\eta}$ along the x direction (Eq. (13)). The horizontal dashed lines indicate the boundary between the connected and disconnected Fermi surfaces. (a) The Fermi surfaces are disconnected in the two regions n and p : four transmission probabilities T_\pm^\pm . (b) The Fermi surfaces are disconnected in region n and partially connected in region p : two transmission probabilities T^\pm when $|k_y| < q_{in}$ and four transmission probabilities T_\pm^\pm when $q_{in} < |k_y| < q_{max}$. (c) The Fermi surfaces are partially connected in region n and disconnected in region p : two transmission probabilities T_\pm when $|k_y| < k_{in}$ and four transmission probabilities T_\pm^\pm when $k_{in} < |k_y| < k_{max}$. (d) The Fermi surfaces are partially connected in the two regions: one transmission probability T when $|k_y| < \min(k_{in}, q_{in})$ and four (T_\pm^\pm) or two (T_\pm or T^\pm) transmission probabilities in the other values of k_y . (e) The Fermi surfaces are connected in the two regions: one transmission probability T .

tudes, we need the matching conditions at the interface $x = 0$. For that, we make the integral and the double integral of the eigenvalue equation $H\Psi(x) = E\Psi(x)$ over

an interval $[-\epsilon, \epsilon]$ by taking $k_x = -i\partial_x$ and sending ϵ to 0 we find:

$$S_x^\varphi \partial_x \Psi(0^+) = S_x^\varphi \partial_x \Psi(0^-) \quad (16a)$$

$$S_x^\varphi \Psi(0^+) = S_x^\varphi \Psi(0^-) \quad (16b)$$

To evaluate the transmission probabilities, we need to introduce the probability current. Starting from the Schrödinger equation $H\Psi = i\hbar\partial_t\Psi$ and using the probability conservation equation $\partial_t |\Psi|^2 + \nabla \cdot \mathbf{J} = 0$, we find:

$$\mathbf{J}[\psi] = \begin{pmatrix} J_x = -\frac{\hbar}{2m} \text{Im} [\partial_x \psi_B^* (\psi_A \cos \varphi + \psi_C \sin \varphi)] \\ \quad + \frac{\hbar}{2m} \text{Im} [\psi_B^* (\partial_x \psi_A \cos \varphi + \partial_x \psi_C \sin \varphi)] \\ J_y = -v_y \text{Im} [\psi_B^* (\psi_A \cos \varphi - \psi_C \sin \varphi)] \end{pmatrix} \quad (17)$$

where $\Psi = (\psi_A, \psi_B, \psi_C)^t$. Note that the matching conditions (Eqs. (16a) and (16b)) correspond to the conservation of the probability current traveling the x axis. All the possibilities for transmission and reflection probabilities are given in Appendix A.

Since we have the transmission probability we can deduce the conductance using the Landauer-Büttiker formula [51]:

$$G_x = 2G_o \sum_{k_y} T_x(k_y) = 2G_o \frac{L_y}{2\pi} \int_{-k_{max}}^{+k_{max}} T_x(k_y) dk_y \quad (18)$$

where T_x is the total transmission probability given from Eq. (A5), $k_{max} = \frac{E}{\hbar v_y}$, L_y is the width of the sample in the y direction, $G_o = \frac{e^2}{h}$ and the factor 2 accounts for the spin degeneracy.

B. Tunneling along the y direction:

Now, the np junction is oriented along the deformation axis (y direction) and is modeled by:

$$V(y) = V_o \Theta(y) \quad (19)$$

where $\Theta(y)$ is the Heaviside step function.

The potential step is uniform along the x direction so that the x component of the wave vector is conserved. The wave function can thus be written as $\Psi(x, y) = \psi(y) e^{ik_x x}$. Solving the Schrödinger equation $[H_o + V(y)] \psi(y) = E\psi(y)$ with the Hamiltonian (6) for a given energy E , transverse momentum k_x and gap parameter Δ , we find two longitudinal momenta k_y^η (q_y^η) in region n (p) which are given by:

$$\begin{aligned} k_y^\eta &= \frac{\eta}{\hbar v_y} \sqrt{E^2 - \left(\Delta + \frac{\hbar^2 k_x^2}{2m}\right)^2} \\ q_y^\eta &= \frac{\eta}{\hbar v_y} \sqrt{(E - V_o)^2 - \left(\Delta + \frac{\hbar^2 k_x^2}{2m}\right)^2} \end{aligned} \quad (20)$$

where $\eta = \pm$ denotes the two longitudinal momenta. The corresponding normalized eigenstates in n and p regions are given by:

$$\psi_n^\eta(y) = \frac{1}{\sqrt{2}} \begin{pmatrix} \cos \varphi e^{i\theta_y^\eta} \\ 1 \\ \sin \varphi e^{-i\theta_y^\eta} \end{pmatrix} e^{ik_y^\eta y} \quad (21a)$$

$$\psi_p^\eta(y) = \frac{1}{\sqrt{2}} \begin{pmatrix} \cos \varphi e^{i\phi_y^\eta} \\ -1 \\ \sin \varphi e^{-i\phi_y^\eta} \end{pmatrix} e^{iq_y^\eta y} \quad (21b)$$

where $\cos \theta_y^\eta = \cos \theta$, $\sin \theta_y^\eta = -\eta \sin \theta$, $\cos \phi_y^\eta = \cos \phi$, $\sin \phi_y^\eta = -\eta \sin \phi$ with θ and ϕ are given from Eq. (11). These phases indicate the direction of the pseudospin in the n and p regions (see Fig. 5) which are given by:

$$\begin{aligned} \langle S_x \rangle_n^\eta &= \langle \psi_n^\eta | S_x^\varphi | \psi_n^\eta \rangle = \cos \theta \\ \langle S_x \rangle_p^\eta &= \langle \psi_p^\eta | S_x^\varphi | \psi_p^\eta \rangle = -\cos \phi \\ \langle S_y \rangle_n^\eta &= \langle \psi_n^\eta | S_y^\varphi | \psi_n^\eta \rangle = \eta \sin \theta \\ \langle S_y \rangle_p^\eta &= \langle \psi_p^\eta | S_y^\varphi | \psi_p^\eta \rangle = -\eta \sin \phi \end{aligned} \quad (22)$$

When k_y^η and q_y^η are real the corresponding group velocities along the y direction in n and p regions are given by:

$$\begin{aligned} v_{yn}^\eta &= \frac{1}{\hbar} \frac{\partial E}{\partial k_y^\eta} = v_y \langle S_y \rangle_n^\eta \\ v_{yp}^\eta &= \frac{1}{\hbar} \frac{\partial (E - V_o)}{\partial k_y^\eta} = v_y \langle S_y \rangle_p^\eta \end{aligned} \quad (23)$$

The group velocities and the pseudospin texture in the two regions n and p are shown in Fig. 5 for different values of the energy E and the gap parameter Δ . The total wave function in the two regions of space is given by:

$$\begin{aligned} \Psi(y < 0) &= \psi_n^+(y) + r\psi_n^-(y) \\ \Psi(y > 0) &= t\psi_p^-(y) \end{aligned} \quad (24)$$

where r and t are respectively the reflection and the transmission amplitudes. In order to determine the matching conditions, we integrate the eigenvalue equation $[H_o + V(y)] \Psi(y) = E\Psi(y)$ over the interval $[-\epsilon, \epsilon]$ by taking $k_y = -i\partial_y$ and sending ϵ to 0 we find:

$$S_y^\varphi \Psi(0^+) = S_y^\varphi \Psi(0^-) \quad (25)$$

This matching condition ensures the conservation of the current probability along the y direction given by Eq. (17). We calculate the transmission amplitude t by using the above matching condition at the interface $y = 0$. Details of the calculation are given in Appendix B. The transmission probability is given by $T_y = \frac{|J_y[\psi_p^-(y < 0)]|}{|J_y[\psi_n^+(y > 0)]|} = \frac{\sin \phi}{\sin \theta} |t|^2$ and is expressed as:

$$T_y = \frac{\beta_+ - \beta_-}{\beta_+} \quad (26)$$

The coefficients β_{\pm} are written as:

$$\beta_{\pm} = (\sin \theta \pm \sin \phi)^2 + \cos^2 2\varphi (\cos \theta + \cos \phi)^2 \quad (27)$$

where θ, ϕ are given from Eq. (11) and the current J_y along the y direction is given from Eq. (17).

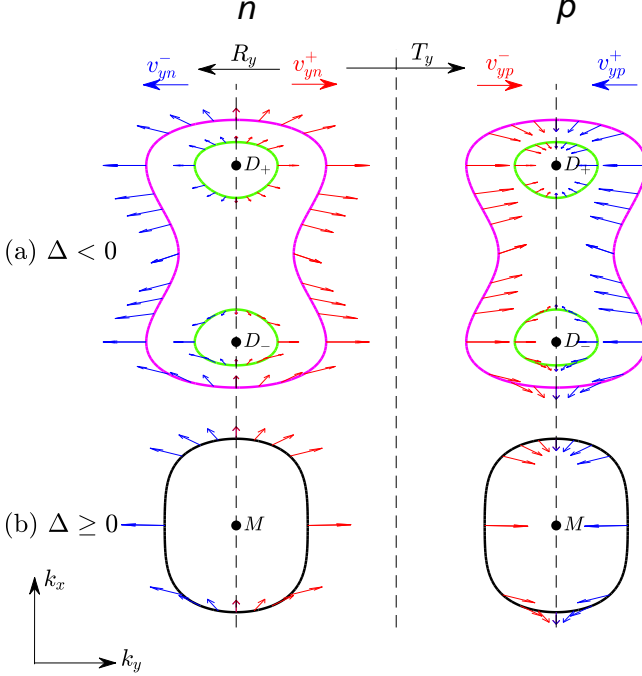


FIG. 5. (Color online) Fermi surfaces topology and pseudospin texture in the two regions n and p . (a) $\Delta < 0$ and for two energies $E < |\Delta|$ (green isoenergy) and $E > |\Delta|$ (magenta isoenergy). (b) $\Delta \geq 0$ and for energy $E > |\Delta|$. Red and blue arrows denote respectively the forward and backward propagation given from the group velocities v_{yn}^{η} and v_{yp}^{η} along the y direction (Eq. (23)). We show the transmission and reflection probabilities T_y and R_y .

Finally, the conductance along the y direction is given by [51]:

$$G_y = 2G_o \sum_{k_x} T_y(k_x) = G_o L_x \frac{2}{\pi} \int_{k_{xmin}}^{k_{xmax}} T_y(k_x) dk_x \quad (28)$$

with

$$k_{xmax} = \sqrt{\frac{2m}{\hbar^2}(E - \Delta)} \quad (29)$$

$$k_{xmin} = \begin{cases} \sqrt{\frac{2m}{\hbar^2}(-E - \Delta)} & \text{if } 0 < E < -\Delta \\ 0 & \text{otherwise} \end{cases}$$

where L_x is the width of the sample in the x direction, $G_o = \frac{e^2}{h}$ and the factor 2 accounts for the spin degeneracy.

IV. RESULTS AND DISCUSSION

In this section, we discuss our results for the different phases illustrated in Fig. 2. We start with the Dirac phase and then we discuss the other phases.

A. The Dirac phase

In this phase the Fermi surfaces are disconnected in the two regions with $0 < E \ll -\Delta$. Hence, the wave vectors given by Eq. (9) can be approximated as $k_{x\eta} \approx q_{x\eta} \approx \sqrt{-\Delta \frac{2m}{\hbar^2}}$. From the expressions of the transmission and reflection probabilities given in Eqs. (A4) and (A2) we can deduce that the intervalley transmission probabilities vanish $T_{-\xi}^{\xi} = 0$. Consequently, the transmission probability \mathcal{T}_x along the x direction in the Dirac phase is the same for the two valleys and is given from the intravalley probabilities as:

$$\mathcal{T}_x = T_+^+ = T_-^- = 1 - \frac{\gamma_-}{\gamma_+} \quad (30)$$

where the coefficients γ_{\pm} are given from Eq. (A3). This transmission probability reproduces the one obtained by E. Illes *et al.* [10] in undeformed $\alpha - T_3$ model ($\lambda = 1$). If the potential is along the y direction, the transmission probability \mathcal{T}_y is the same as given by Eq. (30) where the subscripts x and y are interchanged. In the following, we consider the valley D_+ . The parameter γ_- plays a crucial role in the transparency of the junction who links the pseudospins $\vec{S}_n^+ = (\langle S_x \rangle_n^+, \langle S_y \rangle_n^+)$ and $\vec{S}_p^- = (\langle S_x \rangle_p^-, \langle S_y \rangle_p^-)$ corresponding to the forward propagations in the two regions as shown in red arrows in Fig. 3 (a) for the valley D_+ . Using Eq. (12), the parameter γ_- reads:

$$\gamma_- = \left(\langle S_x \rangle_n^+ - \langle S_x \rangle_p^- \right)^2 + \cos^2 2\varphi \left(\langle S_y \rangle_n^+ - \langle S_y \rangle_p^- \right)^2 \quad (31)$$

The perfect transmission across the np junction ($\mathcal{T}_x = 1$) occurs only if $\gamma_- = 0$ which gives the conditions:

$$\langle S_x \rangle_n^+ = \langle S_x \rangle_p^- \Rightarrow \cos \theta = \cos \phi$$

$$\cos 2\varphi \left(\langle S_y \rangle_n^+ - \langle S_y \rangle_p^- \right) = 0 \Rightarrow \cos 2\varphi (\sin \theta + \sin \phi) = 0 \quad (32)$$

From these equations and using Eq. (11) there are two possibilities to get a perfect transmission:

(i) at normal incidence ($k_y = 0$) regardless of the values of the energy E , the parameter α and the gap parameter Δ .

(ii) for $\phi = \pi/4$ ($\alpha = 1$) and $E = V_o/2$ regardless of the values of the incidence angle and the gap parameter Δ .

The first case, named the KT, is due to the conservation of pseudospin 1/2 for the HCL and the conservation of

pseudospin 1 for the dice lattice. However in the case where $0 < \alpha < 1$, it is due to the conservation of the hybrid pseudospin [22] S_x^φ (Eq. (7)) as shown in Fig. 6. The second case, which is known as the SKT found in the undeformed dice lattice ($\lambda = 1$) [12], is related to the conservation of the pseudospin only along the x direction (see Fig. 6). This behavior can be understood from the boundary conditions [15] given from Eq. (16b) in the Dirac phase. These conditions require the continuity of ψ_B and $\cos\varphi\psi_A + \sin\varphi\psi_C$. For the dice lattice ($\alpha = 1$), the second condition is proportional to $\cos\theta = \langle S_x \rangle$ which means that only the continuity of the x component of the pseudospin is required. We obtain the same results when the potential step is along the y direction except that its transparency is governed by the conservation of the y component of the pseudospin.

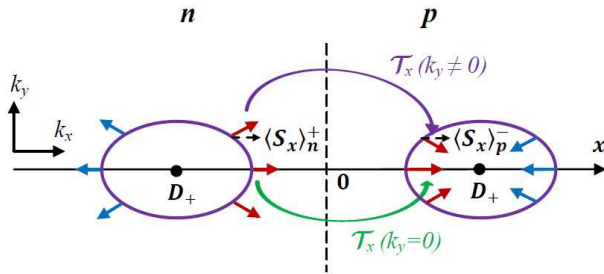


FIG. 6. (Color online) Illustration of the transmission probabilities through a np junction in deformed dice lattice ($\alpha = 1$) for $E = V_o/2$. The arrows represent the orientation of the pseudospins. Red and blue denote the forward and backward propagation respectively given from the group velocities along the x direction (Eq. (13)). At normal incidence ($k_y = 0$), the transparency of the junction (KT) is a consequence of the conservation of the pseudospin. However, at oblique incidence ($k_y \neq 0$), the SKT is a consequence of the conservation of the x component of the pseudospin (dashed black arrows).

Let us now discuss the effects of the deformation and the parameter α on the transmission probability (Eq. (30)). In order to simplify the problem, we study the transparency of the junction at $E = V_o/2$ and using Eq. (A3) and Eq. (11) the transmission probability across a potential step oriented along the $x(y)$ direction reads:

$$\mathcal{T}_{x(y)} = \frac{1}{1 + \frac{v_y^2(x)}{v_x^2(y)} \cos^2 2\varphi \tan^2 \theta_k^{x(y)}} \quad (33)$$

where $\theta_k^{x(y)} = \arctan(k_{y(x)}/k_{x(y)})$ is the incidence angle and the velocities v_x and v_y are given from Eq. (4). In Fig. 7 we present polar plots of the transmission probabilities \mathcal{T}_x and \mathcal{T}_y for the Dirac fermion scattered by np junction along the two directions for $\lambda = 1.2$, $E = V_o/2$ and different values of the parameter α . As mentioned previously, we observe a perfect transmission at normal incidence (KT) for all the cases and the SKT for $\alpha = 1$. We see from Eq. (33) that the transmission probability along the two directions (\mathcal{T}_x or \mathcal{T}_y) increases when

$\alpha = \tan\varphi$ increases as shown in Fig. 7. For a given $\alpha \neq 1$ and $\theta_k^{x(y)} \neq 0$, the junction is more transparent along the deformed y axis $\mathcal{T}_y > \mathcal{T}_x$ due to the fact that $v_x < v_y$ (see Eq. (4)).

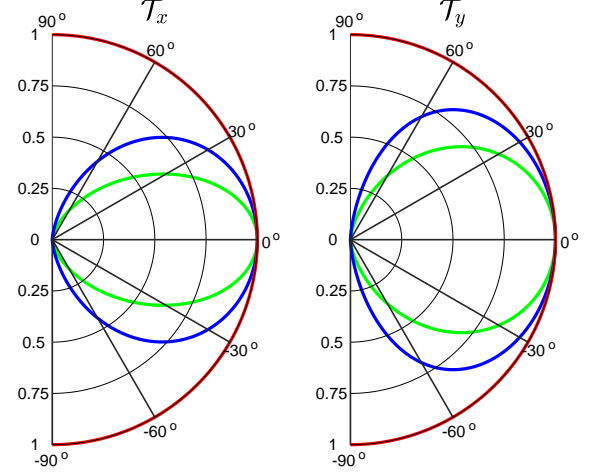


FIG. 7. (Color online) Polar plot of the transmission probabilities \mathcal{T}_x and \mathcal{T}_y through a np junction as a function of the incidence angle for $\lambda = 1.2$, $E = V_o/2$ and different values of α (green for $\alpha = 0$, blue for $\alpha = \frac{1}{\sqrt{3}}$ and red for $\alpha = 1$). The step is of height $V_o = 0.1t$ for the two orientations.

To extend the study for all values of the energy E , we plot in Fig. 8 the conductances G_x and G_y (Eqs. (18), (28)) as a function of the energy E for $\lambda = 1.2$ which are compared to the undeformed case ($\lambda = 1$) and for three values of the parameter α . From Eq. (18) (Eq. (28)) and using the change of variable $k'_y = v_y k_y$ ($k'_x = v_x k_x$), the conductance along the $x(y)$ direction in the Dirac phase is expressed as:

$$G_{x(y)}(\lambda \neq 1) = \frac{v_F}{v_{y(x)}} G(\lambda = 1) \quad (34)$$

where $G(\lambda = 1)$ is the isotropic conductance of the undeformed system. Therefore, the conductance $G_{x(y)}$ decreases (increases) with increasing λ as shown in Fig. 8. We see from this figure that the conductance is maximal at $E = V_o/2$. This behavior is related to the conservation of the x component of the pseudospin ($\cos\theta = \cos\phi \Rightarrow \langle S_x \rangle_n^+ = \langle S_x \rangle_p^-$) which reduces the parameter γ_- and hence the transmission probability (Eq. (30)) reaches a maximum. Particularly, for the dice lattice ($\alpha = 1$), the conductance presents a Λ -shaped peak at $E = V_o/2$ which indicates the SKT regime as the case of the undeformed dice lattice [49]. In this case the conductance takes the value:

$$G_{x(y)}^{SKT} = 4G_o L_{y(x)} \frac{V_o}{2\pi\hbar v_{y(x)}} \quad (35)$$

The factor 4 accounts for the spin and valley degeneracy. We conclude that the electronic transport properties in

the Dirac phase for the deformed $\alpha - T_3$ lattice is similar to the undeformed case. This behavior is related to the fact that the particles behave as massless Dirac fermions in this phase.

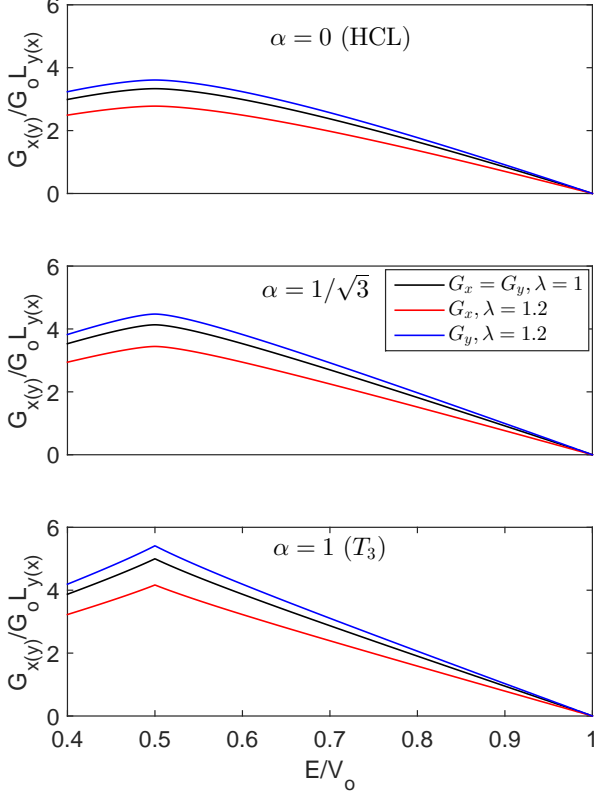


FIG. 8. (Color online) The conductance along the two directions as a function of the energy for three values of the parameter α . For each α , we plot the conductance along the x (red line) and y (blue line) directions for $\lambda = 1.2$ which we compare to the undeformed case (black line with $\lambda = 1$). The step is taken with height $V_o = 0.1t$ for the two orientations.

B. The semi-Dirac and gapped phases

Along the x direction the Dirac fermions traveling the junction are either massive (gapped phase) or the admixture of massless and massive particles (semi-Dirac phase). However, in the y direction only the massless particles travel the junction. We will discuss our results for each case.

1. Tunneling along the x direction:

We plot in Fig. 9 (a) the conductance G_x (Eq. (18)) as a function of Δ/E_o with a fixed energy $E_o = V_o/2$

and for different values of the parameter α . The conductance G_x is normalized to the conductance G_x^{SKT} of the SKT regime in the Dirac phase given by (Eq. (35)). The KT and the SKT disappear for $\Delta > \Delta_o$ indicating the boundary between the Dirac and the semi-Dirac phases.

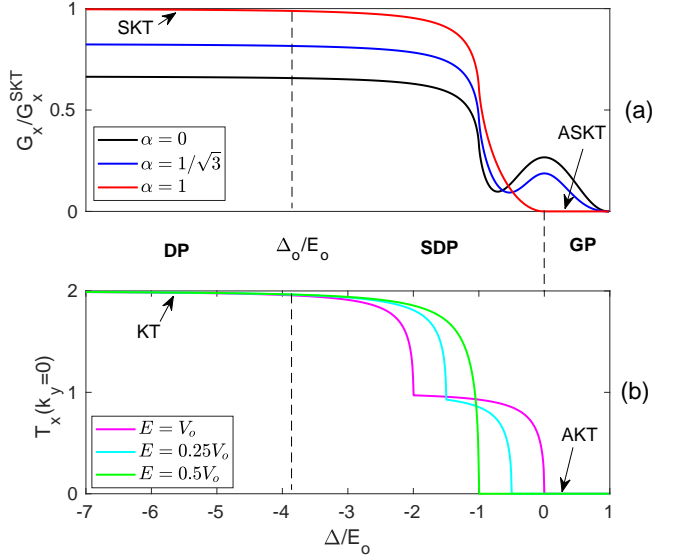


FIG. 9. (Color online) (a) The conductance in unit of G_x^{SKT} as a function of Δ/E_o ($E_o = V_o/2$) and for the three values of α . (b) Transmission probability at normal incidence which is independent of the parameter α and for the three values of the energy E . Note that $T_x(k_y = 0, E) = T_x(k_y = 0, V_o - E)$. We show the three phases: Dirac phase (DP), semi-Dirac phase (SDP) and gapped phase (GP). Here, G_x^{SKT} is the conductance of the SKT regime in the Dirac phase (Eq. (35)). The step is taken with height $V_o = 0.1t$.

When $\Delta < \Delta_o$ we are in the Dirac phase discussed above where the two cones are disconnected with a linear dispersion and only massless particles travel the step with the probability $T_x = 2\mathcal{T}_x$ where \mathcal{T}_x is given by Eq. (30). The SKT and KT regimes are shown respectively in Fig. 9 (a) and (b).

In the gapped phase ($E > \Delta \geq 0$), the two Fermi surfaces merge and the dispersion relation along the x direction is quadratic which means that the particles traveling the junction are massive. In this case the total transmission probability given by Eq. (A5), can be simplified when $E = V_o/2$ as:

$$T_x = \frac{16q_o^2 q_+^2 (\gamma_+ - \gamma_-) \gamma_-}{\gamma_+^2 (q_+^2 + q_o^2)^2} \quad (36)$$

where $q_o = -ik_{x-}$, $q_+ = k_{x+}$ (see Eq. (9)) and γ_{\pm} is given from Eq. (A3). At normal incidence we get a perfect reflection for all values of the parameter α and the energy $0 < E < V_o$ as depicted in Fig. 9(b). This behavior, known as AKT, is a consequence of the conservation of the pseudospin between the incident and reflected

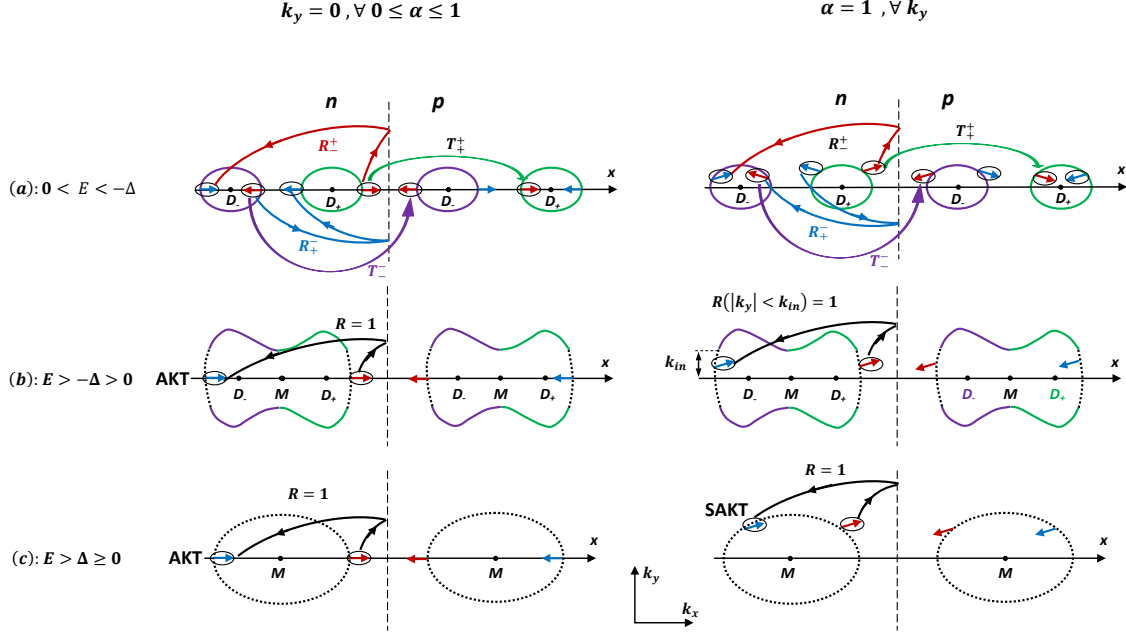


FIG. 10. (Color online) Illustration of the transmission probabilities in the semi-Dirac and gapped phases for $E = V_o/2$. The arrows represent the orientation of the pseudospin. Red and blue denote respectively the forward and backward propagation given from the group velocities along the x direction (Eq. (13)). Left: at normal incidence ($k_y = 0$) and for all values of α . Right: $\alpha = 1$ and for all values of the incidence angle (k_y). (a) Sub-phase (i) (see text): the intervalley reflection R_{\pm}^{\mp} destroys the perfect transmission (KT in the left or SKT in the right). (b) Sub-phase (ii) (see text): perfect reflection at normal incidence (AKT) (left) while a perfect reflection for $k_y \neq 0$ (right) occurs only when the Fermi surfaces are connected ($|k_y| < k_{in}$). (c) Gapped phase: perfect reflection at normal incidence (AKT on the left) and a perfect reflection for all k_y (SAKT on the right). The transparency of the junction at normal incidence is a consequence of the conservation of the pseudospin. However, at oblique incidence ($k_y \neq 0$) and for $\alpha = 1$, the transparency of the junction is a consequence of the conservation of the x component of the pseudospin.

waves as illustrated in Fig. 10(c). This behavior is also related to the fact that the pseudospins of the incident and transmitted waves are antiparallel [30]. Indeed, the parameter γ_- links the pseudospins corresponding to the forward propagations in the two regions as shown in red arrows in Fig. 3 (c) and reads:

$$\gamma_- = \left(\langle S_x \rangle_n^+ + \langle S_x \rangle_p^+ \right)^2 + \cos^2 2\varphi \left(\langle S_y \rangle_n^+ - \langle S_y \rangle_p^+ \right)^2 \quad (37)$$

At normal incidence the parameter $\gamma_- = 0$ which leads to antiparallel pseudospins: $\langle S_x \rangle_n^+ = -\langle S_x \rangle_p^+$. In the case of the dice lattice ($\alpha = 1$) and for $E = V_o/2 > \Delta$ the transmission probability vanishes for all the incident angles despite the presence of states at the interface of the junction. This regime is the counterpart of the SKT found in the Dirac phase which is called anti-super Klein tunneling (ASKT) [30]. In this case, the parameter $\gamma_- = 0$ which means that the x components of the pseudospins of the incident and transmitted waves are antiparallel. Hence, the x components of the pseudospins between the incident and reflected waves is conserved for all the incident angles as depicted in Fig. 10(c). The behavior of the conductance as a function of α in the gapped phase is opposite to that in the Dirac phase as

depicted in Fig. 9(a) where the junction becomes more transparent when α decreases which is a consequence of the pseudospin conservation and the nature of particles in the two phases.

In the semi-Dirac phase ($\Delta_o < \Delta \leq 0$ and $E \sim |\Delta|$) there are two sub-phases:

(i) for $E \lesssim -\Delta$ the Fermi surfaces are disconnected (see Fig. 3 (a)) but the dispersion relation is not linear around the Dirac points D_{\pm} (see Eq.(3)) which means that the current along the x direction is a mixture of massive and massless particles traveling the junction. In this case the transmission and reflection probabilities (Eq. (A4)) at $E = V_o/2$ can be expressed as:

$$T_{\xi}^{\xi} = \frac{4q_+q_-(\gamma_+ - \gamma_-)}{\gamma_+(q_+ + q_-)^2}, \quad R_{-\xi}^{\xi} = \frac{(q_+ - q_-)^2}{(q_+ + q_-)^2} \quad (38)$$

$$R_{\xi}^{\xi} = \frac{4q_+q_-\gamma_-}{\gamma_+(q_+ + q_-)^2}, \quad T_{-\xi}^{\xi} = 0$$

where $q_{\pm} = k_{x\pm}$ for $E = V_o/2$ (see Eq. (9)). At normal incidence ($k_y = 0$) or for $\alpha = 1$ the parameter $\gamma_- = 0$ which is related to the conservation of the x component of the pseudospin as previously discussed in the Dirac and gapped phases. In this case, the transmission

and reflection probabilities (Eq.(38)) become:

$$\begin{aligned} T_\xi^\xi &= \frac{4q_+q_-}{(q_+ + q_-)^2}, \quad R_{-\xi}^\xi = \frac{(q_+ - q_-)^2}{(q_+ + q_-)^2} \\ R_\xi^\xi &= T_{-\xi}^\xi = 0 \end{aligned} \quad (39)$$

When the two Fermi surfaces get closer, the intervalley reflections $R_{-\xi}^\xi$ emerge due to the pseudospin conservation (see Fig. 10 (a)) and causes the disappearance of the KT and the SKT.

(ii) for $E \gtrsim -\Delta$ the Fermi surfaces merge when $|k_y| < k_{in} = \frac{\sqrt{E^2 - \Delta^2}}{\hbar v_y}$ where the particles are massive and disconnected when $k_{in} < |k_y| < k_{max} = \frac{E}{\hbar v_y}$ (see Fig. 3 (b)) where we get a mixture of massive and massless particles traveling the junction. The transmission and reflection probabilities at $E = V_o/2$ are given from Eq. (36) when the Fermi surfaces are connected and from Eq. (38) when they are disconnected. A perfect reflection occurs when the Fermi surfaces are connected and particularly at normal incidence where we get the AKT regime. When the Fermi surfaces are disconnected there is no perfect reflection as in the sub-phase (i) and then we cannot get the ASKT regime (see Fig. 10 (b)). However, notice that the conductance exhibits two opposite behaviors as a function of the parameter α as shown in Fig. 9 (a). Firstly, the junction is more transparent when α increases as in the Dirac phase. This means that the current along the x direction is dominated by massless particles. Secondly, the junction becomes less transparent when α increases as in the gapped phase which indicates the dominance of massive particles. One can see from Fig. 9 (b) a transition from KT to AKT for all values of the energy $0 < E < V_o$ and the parameter α as the case of the deformed HCL ($\alpha = 0$) [27]. Likewise, a transition from SKT to ASKT occurs in the deformed dice lattice ($\alpha = 1$) for energy $E = V_o/2$.

In what follows, we examine the dependence of the conductance on the energy in the gapped phase. We plot in Fig. 11 the conductance G_x (in unit of G_x^{SKT}) as a function of the energy E for $\Delta = 0$ and for different values of the parameter α . The conductance is enhanced with decreasing α for all values of the energy. Particularly, at $E = V_o/2$ the conductance vanishes for $\alpha = 1$ indicating the ASKT regime.

With the increase of α , the conductance shows a transition from a maximum to a minimum around $E = V_o/2$. This effect can be understood as a competition between two effects. Firstly, the particles can travel through the junction only if the wave vectors k_{x+} and q_{x+} (Eq. (9)) are both real. Consequently, the allowed range of incident angles (as controlled by k_y) is maximum at $E = V_o/2$, which leads to a maximum conductance. Secondly, the transmission probability at $E = V_o/2$ (Eq. 36) (and subsequently the conductance) decreases as α increases as a result of the conservation of the pseudospin via the γ_- parameter.

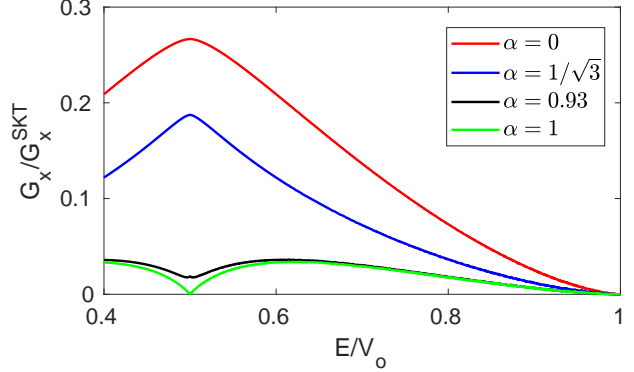


FIG. 11. (Color online) Conductance along the x direction of the deformed $\alpha - T_3$ lattice for $\Delta = 0$ as a function of the energy and for four values of the parameter α . The step is taken with height $V_o = 0.1t$.

2. Tunneling along the y direction:

When the potential step is along the y direction (deformation direction), the dispersion relation is linear for any value of the gap parameter Δ (see Fig. 2) and hence the particles traveling the junction are massless. Therefore, the tunneling along the y direction is similar to that along the x direction in the Dirac phase. Indeed, from the expression of the transmission probability T_y along the y direction (Eq. (26)), the perfect transmission ($T_y = 1$) occurs if $\beta_- = 0$ (Eq. (27)) which is related to the pseudospin conservation:

$$\begin{aligned} \sin \theta &= \sin \phi \Rightarrow \langle S_y \rangle_n^+ = \langle S_y \rangle_p^- \\ \cos 2\varphi (\cos \theta + \cos \phi) &= 0 \Rightarrow \cos 2\varphi \left(\langle S_x \rangle_n^+ - \langle S_x \rangle_p^- \right) = 0 \end{aligned} \quad (40)$$

where the components of the pseudospin are given by Eq. (22).

There are two possibilities to get a perfect transmission:

(i) At normal incidence for $k_x = \pm \sqrt{\frac{-2m}{\hbar^2} \Delta}$ when $\Delta < 0$ (Fig. 12 (a)) and $k_x = 0$ when $\Delta \geq 0$ (Fig. 12 (b)) for all values of the parameter α and the energy $E < V_o$. This perfect transmission is referred to KT which arises from the pseudospin conservation.

(ii) The regime of the SKT which happens for the deformed dice lattice ($\alpha = 1$) at $E = V_o/2$, is related to the conservation of the y component of the pseudospin $\langle S_y \rangle_n^+ = \langle S_y \rangle_p^-$ (dashed arrow in Fig. 12).

We show in Fig. 13 the conductance along the y direction (Eq. (28)) in unit of the conductance in the SKT regime: $G_y^{SKT} = G_o L_x \frac{2}{\pi} (k_{xmax} - k_{xmin})$ where k_{xmax} and k_{xmin} are given from Eq. (29). In Fig. 13 (a) the conductance is plotted as a function of E/V_o for $\Delta = 0$. For $\alpha = 1$, the conductance presents a Λ -shaped peak at $E = V_o/2$ which indicates the SKT regime [49] as the case of the conductance along the x direction in the Dirac phase. We plot in Fig. 13 (b) the conductance as

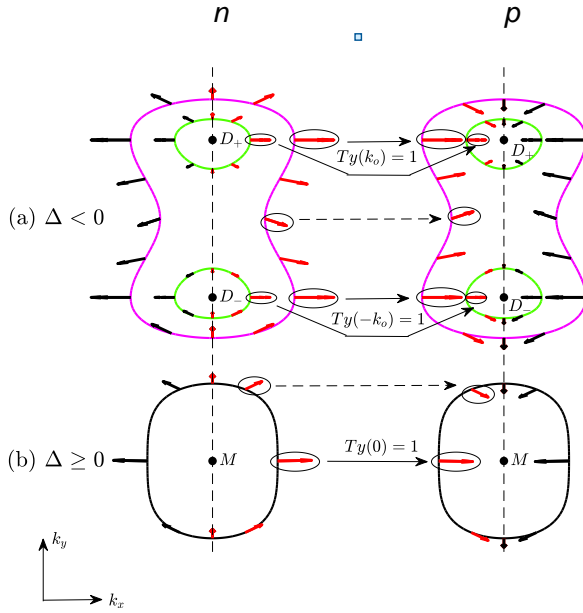


FIG. 12. (Color online) Schematic representation of the transmission probabilities along the y direction for different values of the gap parameter Δ . The arrows represent the orientation of the pseudospin (Eq. (22)). Red and blue denote respectively the forward and backward propagation given from the group velocities along the y direction (Eq. (23)). (a) $E > -\Delta > 0$ (magenta isoenergy) and $0 < E < -\Delta$ (green isoenergy). The perfect transmission at normal incidence ($k_x = \pm k_o$) is a consequence of the pseudospin conservation. For, $E = V_o/2$ and $\alpha = 1$ we get a perfect transmission at any incidence angle (SKT) which is related to the conservation of the y component of the pseudospin (dashed arrow). Here $k_o = \pm \sqrt{\frac{-2m}{\hbar^2}} \Delta$. (b) $E > \Delta \geq 0$. The perfect transmission at normal incidence ($k_x = 0$) is a consequence of the pseudospin conservation and the SKT regime as in (a).

a function of Δ/E with a fixed energy $E = V_o/2$. The SKT regime occurs in all the phases for $\alpha = 1$ which is related to the linear dispersion along the y direction as depicted in Fig. 2. Finally, the conductance increases with increasing α as the case of the conductance along the x direction in the Dirac phase. Note that, a transition from KT to AKT or from SKT to ASKT can be done in the gapped phase by the rotation of the junction

V. CONCLUSIONS

In this work we have investigated the effect of a uniaxial deformation on the tunneling across a np junction for the $\alpha - T_3$ model. We have showed that the Dirac cones move toward each other and merge under a compressive deformation while the flat band remains unchanged. At moderate deformation (in the Dirac phase), we have found that the transparency of the np junction in any

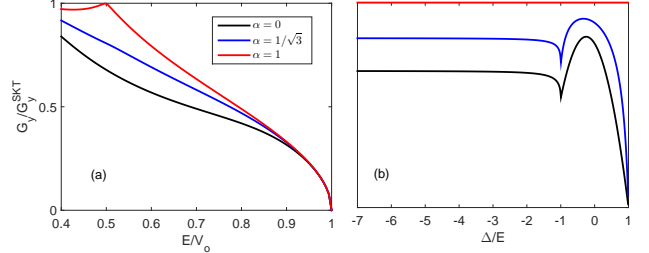


FIG. 13. (Color online) Conductance along the y direction in unit of the conductance G_y^{SKT} in the SKT regime and for three values of α . (a) Conductance as a function of E/V_o with $\Delta = 0$. (b) Conductance as a function of Δ/E with a fixed energy $E = V_o/2$. The step is taken with height $V_o = 0.1t$.

direction and for all energies increases with the parameter α and the step becomes perfectly transparent at normal incidence (KT) for all values of α and the energy $0 < E < V_o$. Particularly, for the dice lattice ($\alpha = 1$) and for an energy equal to half of the step height, the junction is fully transparent (SKT) in the Dirac phase. These results have already been showed in undeformed $\alpha - T_3$ lattice which can be explained by the fact that the particles behave as massless fermions in the Dirac phase. We have demonstrated that the SKT regime in the dice lattice is related to the conservation of the longitudinal pseudospin component.

When the Fermi surfaces merge, under the effect of the deformation, the particles traveling the np junction perpendicular to the deformation direction behave as massive fermions which are totally reflected at normal incidence regardless of the values of α and the energy. This AKT effect is a consequence of the pseudospin conservation. In the deformed dice lattice ($\alpha = 1$) and for an energy equal to half of the step height, the np junction is fully opaque when the Fermi surfaces merge totally (in the gapped phase). This SAKT effect is due to the fact that the longitudinal components of the pseudospins of the incident and transmitted waves are antiparallel. We have seen in the gapped phase that the transparency of the np junction perpendicular to the deformation direction decreases when α increases in contrast to the case where it is oriented along the other direction.

The particles traveling the np junction parallel to the deformation direction behave as massless fermions in all the phases. Therefore, all the tunneling properties as the KT and the SKT remain valid for any strength of deformation. Finally, a transition from the KT (SKT) to the AKT (SAKT) can be realized by the rotation of the junction in the gapped phase or by a continuous uniaxial deformation perpendicular to the junction.

ACKNOWLEDGMENTS

We gratefully acknowledge J.-N. Fuchs for helpful discussions and for a critical reading of the manuscript. This work was partially supported by the Tunisian-French CMCU 15G1306 project.

Appendix A: The total transmission probability along the x direction:

The total transmission probability depends on the topology of the Fermi surfaces in the two regions, as depicted in Fig. 4, which can be summarized in four situations:

(i) The two Fermi surfaces are disconnected in the two regions n and p with four transmission amplitudes t_ξ^ξ and $t_{-\xi}^\xi$ where $\xi = \pm$ is the valley index (Fig. 4 (a)). By applying the matching conditions (Eq. (16a) and Eq. (16b)) at $x = 0$ for the total wave function given from Eq. (15), we obtain a system of four equations:

$$\begin{aligned} 1 + r_\xi^\xi + r_{-\xi}^\xi &= -t_\xi^\xi - t_{-\xi}^\xi \\ a^\xi + a^{-\xi} r_\xi^\xi + a^\xi r_{-\xi}^\xi &= b^{-\xi} t_\xi^\xi + b^\xi t_{-\xi}^\xi \\ k_\xi + k_{-\xi} r_\xi^\xi - k_\xi r_{-\xi}^\xi &= -q_{-\xi} t_\xi^\xi + q_\xi t_{-\xi}^\xi \\ a^\xi k_\xi + a^{-\xi} k_{-\xi} r_\xi^\xi - a^\xi k_\xi r_{-\xi}^\xi &= b^{-\xi} q_{-\xi} t_\xi^\xi - b^\xi q_\xi t_{-\xi}^\xi \end{aligned} \quad (\text{A1})$$

where $a^\xi = \xi \cos \theta - i \cos 2\varphi \sin \theta$ and $b^\xi = \xi \cos \phi - i \cos 2\varphi \sin \phi$ with θ and ϕ given from Eq. (11). The wave vectors $k_\xi = k_{x\xi}$ and $q_\xi = q_{x\xi}$ are given by Eq. (9). We omit the index x for simplicity. By solving these equations, we obtain the transmission and reflection amplitudes:

$$\begin{aligned} t_\xi^\xi &= \frac{-2k_\xi (a^\xi - a^{-\xi}) (a^\xi + b^\xi) (k_{-\xi} + q_\xi)}{\gamma_+ (k_\xi + q_{-\xi}) (k_{-\xi} + q_\xi) - \gamma_- (k_{-\xi} - q_{-\xi}) (k_\xi - q_\xi)} \\ t_{-\xi}^\xi &= \frac{2k_\xi (a^\xi - a^{-\xi}) (a^\xi + b^{-\xi}) (k_{-\xi} - q_{-\xi})}{\gamma_+ (k_\xi + q_{-\xi}) (k_{-\xi} + q_\xi) - \gamma_- (k_{-\xi} - q_{-\xi}) (k_\xi - q_\xi)} \\ r_\xi^\xi &= \frac{2k_\xi (a^\xi + b^{-\xi}) (a^\xi + b^\xi) (q_+ + q_-)}{\gamma_+ (k_\xi + q_{-\xi}) (k_{-\xi} + q_\xi) - \gamma_- (k_{-\xi} - q_{-\xi}) (k_\xi - q_\xi)} \\ r_{-\xi}^\xi &= \frac{\gamma_+ (k_\xi - q_{-\xi}) (k_{-\xi} + q_\xi) - \gamma_- (k_{-\xi} - q_{-\xi}) (k_\xi + q_\xi)}{\gamma_+ (k_\xi + q_{-\xi}) (k_{-\xi} + q_\xi) - \gamma_- (k_{-\xi} - q_{-\xi}) (k_\xi - q_\xi)} \end{aligned} \quad (\text{A2})$$

where γ_\pm is given by:

$$\gamma_\pm = (\cos \theta \pm \cos \phi)^2 + \cos^2 2\varphi (\sin \theta + \sin \phi)^2 \quad (\text{A3})$$

(ii) The two Fermi surfaces are connected in the two regions (Fig. 4 (d), (e)): there is only one transmission amplitude $t = t_+^+$ and one reflection amplitude $r = r_-^+$ where t_+^+ and r_-^+ are given from Eq. (A2) by replacing k_- with $-k_-$.

(iii) The two Fermi surfaces are connected in the region n and are disconnected in the region p (Fig. 4 (c)): there are two transmission amplitudes $t_+ = t_+^+$ and $t_- = t_-^+$

and one reflection amplitude $r = r_-^+$ given from Eq. (A2) by replacing k_- with $-k_-$.

(iv) The two Fermi surfaces are disconnected in the region n and have merged in the region p (Fig. 4 (b)): there are two transmission amplitudes $t^+ = t_+^-$ and $t^- = t_-^-$ and four reflection amplitudes r_ξ^ξ and $r_{-\xi}^\xi$ ($\xi = \pm$) that are given from Eq. (A2). The transmission and reflection probabilities are given by:

$$\begin{aligned} T_\xi^\xi &= \frac{|J_x [\psi_p^{\xi-\xi}(x > 0)]|}{|J_x [\psi_n^{\xi\xi}(x < 0)]|} = \left| \frac{q_{-\xi} \cos \phi}{k_\xi \cos \theta} \right| |t_\xi^\xi|^2 \\ T_{-\xi}^\xi &= \frac{|J_x [\psi_p^{-\xi\xi}(x > 0)]|}{|J_x [\psi_n^{\xi\xi}(x < 0)]|} = \left| \frac{q_\xi \cos \phi}{k_\xi \cos \theta} \right| |t_{-\xi}^\xi|^2 \\ R_\xi^\xi &= \frac{|J_x [\psi_n^{\xi-\xi}(x < 0)]|}{|J_x [\psi_n^{\xi\xi}(x < 0)]|} = \left| \frac{k_{-\xi}}{k_\xi} \right| |r_\xi^\xi|^2 \\ R_{-\xi}^\xi &= \frac{|J_x [\psi_n^{-\xi\xi}(x < 0)]|}{|J_x [\psi_n^{\xi\xi}(x < 0)]|} = |r_{-\xi}^\xi|^2 \end{aligned} \quad (\text{A4})$$

The current J_x is given from Eq. (17) and the wave functions $\psi_{n,p}^{\xi\xi'}(x)$ from Eqs. (10a) and (10b). Finally, the total transmission probability along the x direction is given by:

$$T_x = \begin{cases} T_+^+ + T_-^+ + T_+^- + T_-^- & \text{situation (i)} \\ T & \text{situation (ii)} \\ T_+ + T_- & \text{situation (iii)} \\ T^+ + T^- & \text{situation (iv)} \end{cases} \quad (\text{A5})$$

Appendix B: The transmission amplitude along the y direction:

Applying the matching conditions (Eq. (25)) at $x = 0$ for the total wave function given from Eq. (24), we obtain a system of two equations:

$$\begin{aligned} 1 + r &= -t \\ a^+ + a^- r &= b^- t \end{aligned} \quad (\text{B1})$$

where $a^\pm = \cos 2\varphi \cos \theta \mp i \sin \theta$ and $b^- = \cos 2\varphi \cos \phi + i \sin \phi$ with θ and ϕ given from Eq. (11). Straight forward, the transmission amplitude is given by:

$$t = \frac{a^+ - a^-}{b^- + a^-} \quad (\text{B2})$$

* Electronic address: lassaad.mandhour@istmt.utm.tn

[1] O. Klein, *Z. Phys.* **53**, 157 (1929).

[2] A. Calogeracos, N. Dombey, *Contemp. Phys.* **40**, 313 (1999).

[3] Dombey, N. C., A. Seventy years of the Klein paradox. *Phys. Rep.* **315**, 41 (1999).

[4] K. S. Novoselov, A. K. Geim, S. V. Morozov, D. Jiang, Y. Zhang, S. V. Dubonos, I. V. Grigorieva and A. A. Firsov, *Science* **306**, 666 (2004).

[5] B. Huard, J. A. Sulpizio, N. Stander, K. Todd, B. Yang, and D. Goldhaber-Gordon, *Phys. Rev. Lett.* **98**, 236803 (2007).

[6] N. Stander, B. Huard, and D. Goldhaber-Gordon, *Phys. Rev. Lett.* **102**, 026807 (2009).

[7] A.F. Young, P. Kim, *Nature Phys.* **5**, 222 (2009).

[8] M. I. Katsnelson, K. S. Novoselov and A. K. Geim, *Nature Phys.* **2**, 620 (2006).

[9] P.E. Allain, and J.N. Fuchs, *Eur. Phys. J.* **B83**, 301 (2011).

[10] E. Illes and E. J. Nicol, *Phys. Rev. B* **95**, 235432 (2017).

[11] Z. Lan, N. Goldman, A. Bermudez, W. Lu and P. Öhberg, *Phys. Rev. B* **84**, 165115 (2011).

[12] D.F. Urban, D. Bercioux, M. Wimmer and W. Häusler, *Phys. Rev. B* **84**, 115136 (2011).

[13] K. Kim, *Results Phys.* **12**, 1391 (2019).

[14] Y. Betancur-Ocampo, G. Cordourier-Maruri, V. Gupta, and R. de Coss, *Phys. Rev. B* **96**, 024304 (2017).

[15] A. Fang, Z.Q. Zhang, S.G. Louie and C.T. Chan, *Phys. Rev. B* **93**, 035422 (2016).

[16] R. Shen, L. B. Shao, B. Wang and D. Y. Xing, *Phys. Rev. B* **81**, 041410(R) (2010).

[17] Y. Betancur-Ocampo, *J. Phys.: Condens. Matter* **30**, 435302 (2018).

[18] B. Sutherland, *Phys. Rev. B* **34**, 5208 (1986).

[19] J. Vidal, R. Mosseri and B. Doucot, *Phys. Rev. Lett.* **81**, 5888 (1998).

[20] D. Bercioux, D. F. Urban, H. Grabert, and W. Häusler, *Phys. Rev. A* **80**, 063603 (2009).

[21] A. Raoux, M. Morigi, J.-N. Fuchs, F. Piéchon, and G. Montambaux, *Phys. Rev. Lett.* **112**, 026402 (2014).

[22] E. Illes and E. J. Nicol, *Phys. Rev. B* **94**, 125435 (2016).

[23] J. D. Malcolm and E. J. Nicol, *Phys. Rev. B* **92**, 035118 (2015).

[24] V. Kleptsyn, A. Okunev, I. Schurov, D. Zubov, M. I. Katsnelson, *Phys. Rev. B* **92**, 165407 (2015).

[25] A. Varlet, M. H. Liu, D. Bischoff, P. Simonet, T. Taniguchi, K. Watanabe, K. Richter, T. Ihn, K. Ensslin, *Phys. Status Solidi* **10**, 46 (2016).

[26] R. Du, M.H. Liu, J. Mohrmann, F. Wu, R. Krupke, H.V. Löhneysen, K. Richter, R. Danneau, *Rev. Lett.* **121**, 127706 (2017).

[27] O. Bahat-Treidel, O. Peleg, M. Grobman, N. Shapira, M. Segev, and T. Pereg-Barnea, *Phys. Rev. Lett.* **104**, 063901 (2010).

[28] M.-H. Liu, J. Bundesmann, K. Richter, *Phys. Rev. B* **85**, 085406 (2012).

[29] S. Banerjee and W. E. Pickett, *Phys. Rev. B* **86**, 075124 (2012).

[30] Yonatan Betancur-Ocampo, François Leyvraz, and Thomas Stegmann, *Nano Lett.* **19**, (11), 7760-7769 (2019).

[31] M.O. Goerbig, J.-N. Fuchs, G. Montambaux and F. Piéchon, *Phys. Rev. B* **78**, 045415 (2008).

[32] G. Montambaux, F. Piéchon, J.-N. Fuchs, and M. O. Goerbig, *Eur. Phys. J. B* **72**, 509 (2009).

[33] V. M. Pereira and A. H. Castro Neto and N. M. R. Peres, *Phys. Rev. B* **80**, 045401 (2009).

[34] R. de Gail, J. N. Fuchs, M. O. Goerbig, F. Piechon, and G. Montambaux, *Physica B* **407**, 1948 (2012).

[35] G. Montambaux, F. Piéchon, J.-N. Fuchs, and M. O. Goerbig, *Phys. Rev. B* **80**, 153412 (2009).

[36] L. Tarruell, D. Greif, T. Uehlinger, G. Jotzu and T. Esslinger, *Nature*, **483**, 302 (2012).

[37] J. Feilhauer, W. Apel, and L. Schweitzer, *Phys. Rev. B* **92**, 245424 (2009).

[38] S. Banerjee, R. R. P. Singh, V. Pardo, and W. E. Pickett, *Phys. Rev. Lett.* **103**, 016402 (2009).

[39] M. Polini, F. Guinea, M. Lewenstein, H. C. Manoharan and V. Pellegrini, *Nature Nanotech.* **8**, 625 (2013).

[40] M. Bellec, U. Kuhl, G. Montambaux, and F. Mortessagne, *Phys. Rev. Lett.* **110**, 033902 (2013).

[41] G. Montambaux, *Comptes Rendus Phys.* **19**, 285305 (2018).

[42] Y. Betancur-Ocampo, *Phys. Rev. B* **98**, 205421 (2018).

[43] K. Saha, R. Nandkishore, and S. A. Parameswaran, *Phys. Rev. B* **96**, 045424 (2017).

[44] P. Adroguer, D. Carpentier, G. Montambaux and E. Orignac, *Phys. Rev. B* **93**, 125113 (2016).

[45] Yee Sin Ang, Shengyuan A. Yang, C. Zhang, Zhongshui Ma, and L. K. Ang, *Phys. Rev. B* **96**, 245410 (2017).

[46] M. Van der Donck, F. M. Peeters, and B. Van Duppen, *Phys. Rev. B* **93**, 115423 (2016).

[47] Hao-Fu Zhu, Xue-Qian Yang, Jun Xu and Shuai Cao, *Eur. Phys. J. B* **93**, 4 (2020).

[48] L Dell'Anna, P Majari and M R Setare, *J. Phys.: Condens. Matter* **30** 415301 (2018).

[49] R. Zhu and P. M. Hui, *Phys. Lett. A* **381**, 1971 (2017).

[50] F. Piéchon, J.-N. Fuchs, A. Raoux, and G. Montambaux, *J. Phys.: Conf. Ser.* **603**, 012001 (2015).

[51] Ya.M. Blanter and M. Büttiker, *Phys. Rep.* **336**, 1 (2000).